

國立臺灣大學理學院大氣科學研究所



碩士論文

Graduate Institute of Atmospheric Sciences

College of Science

National Taiwan University

Master Thesis

海洋大陸地區森林砍伐降水反應之氣候平均態相依性

Mean-states Dependence of Deforestation Induced Precipitation

Changes in the Maritime Continent

蔣濬濂

Chun-Lien Chiang

指導教授：羅敏輝 博士

Advisor: Min-Hui Lo, Ph.D.

中華民國 112 年 1 月

January, 2023

誌謝

羅敏輝老師在我學術生涯中的指導跟鼓勵。羅老師總是能在我覺得因研究而困惑、自我懷疑時給予我非常正向的信心激勵。而且讓我逐漸養成越來越自律的生活，以及有成就感的研究體驗。雖然在碩士生涯中，對於科學那種仰之彌高、鑽之彌堅的感受越來越強烈，但每當老師靜下來跟我認真討論時，總能覺得又多進步了一點，長久以來也積累了可觀的收穫。

實驗室的同学、同事們是我這一兩年來的主要生活圈，陪伴我過了許多研究內與研究外的生活。除了在研究上給了我很多精神支持外，在其他的日常生活中，也讓我覺得有一群跟我一樣的朋友們在跟我一起奮鬥。這一切雖然平凡，但是讓我的生活永遠都不會匱乏。謝謝我生活中的各種夥伴。

最後，感謝我的家人做我永遠的精神後盾。

中文摘要



在過往研究中，數值模擬的實驗說明了海洋大陸森林砍伐會造成降水量的顯著變化。然而，森林砍伐的氣候反應與其氣候平均態之間的關聯性仍不清楚。本研究旨在分析在大氣模式比較計畫（AMIP）類型的實驗以及海-陸-氣耦合氣候模式的實驗中，氣候平均態如何調節森林砍伐對氣候系統所造成的降水量反應。我們發現，相對於年代際尺度的長期氣候平均，在海洋大陸陸地區域的大氣溼靜能垂直環境擁有「負凹型」剖面（中對流層溼靜能量值低於氣候平均值，中低對流層之間溼靜能梯度的不穩定度更高）時，森林砍伐有利於更強的溼靜能局部傳送，傾向於引發更多的年降水量增加。森林砍伐所引起的降水增加也透過負回饋機制降低了海洋大陸陸地區域的年際降水變異度。相對於長期氣候平均，在更乾、更少雨的氣候狀態下，森林砍伐反而讓降水變多。透過本研究提出的機制，可以幫助推估在考慮不同氣候平均態的條件下，地表變遷所引起的地球系統反應。

關鍵字：海洋大陸、森林砍伐、降水年際變異度、氣候平均態、溼靜能、CESM

ABSTRACT

Deforestation leads to significant changes in precipitation in the Maritime Continent.

However, the dependence of deforestation response to the climate mean-states remains unclear. This study investigated how the climate mean-states modulate deforestation-induced precipitation anomalies by performing both Atmospheric Model Intercomparison Project-type and fully coupled climate model simulations. We discovered that the atmospheric environment over the Maritime Continent land regions, having moist static energy with a negative-concave-type vertical profile (lower mid-tropospheric MSE magnitudes related to the climate average, and higher instability in view of MSE gradient between mid- and lower-troposphere) in the mean-state, is favorable to more vigorous local energy transportation and tends to lead to higher precipitation after deforestation relative to the long-term (decadal time-scale) climatological mean. Deforestation-induced precipitation anomalies also reveal negative feedback in which deforestation can modulate interannual variability by increasing precipitation in a drier mean-state. The mechanism proposed in this study can help diagnose the responses in the Earth system caused by land-use change in consideration of different mean-states.

Keywords: Maritime Continent, deforestation, interannual variability of precipitation, climate mean-state, moist static energy, CESM

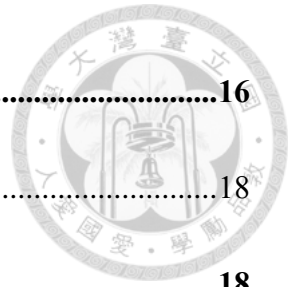


CONTENTS



誌謝	i
中文摘要	ii
ABSTRACT	iii
CONTENTS	iv
LIST OF FIGURES	vi
LIST OF TABLES	x
Chapter 1 Introduction.....	1
Chapter 2 Data and Methodology.....	5
2.1 Model Experiments	5
2.2 Analysis of Moist Static Energy (MSE)	8
2.3 Grouping of Events	10
2.4 Tests of Significance	11
Chapter 3 Results.....	12
3.1 Patterns of Climatological Precipitation in the Maritime Continent	12
3.2 Characteristic of MSE Mean-states	12
3.3 Role of MSE Budget.....	13

3.4	Local Transport of MSE.....	16
Chapter 4	Discussion.....	18
4.1	The Seasonality of Precipitation Responses	18
4.2	Role of Ocean Feedback	18
4.3	Model Test for Long-term Ocean Feedback	20
4.4	Role of Vertical Wind Velocities.....	22
4.5	The Contributors to the Interannual Variabilities of MSE Profiles..	23
4.6	Features of Simulation using Global Climate Model.....	25
Chapter 5	Conclusion	26
FIGURES	28
TABLES	40
REFERENCES	42



LIST OF FIGURES

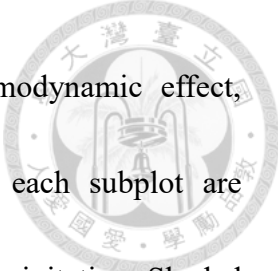


Figure 1. Seasonal cycle of precipitation in (a) CTL and (b) ANO run (Wm^{-2}) in prescribed-SST simulation. Horizontal axis is month and starts from July to June next year. Shaded area represents confident interval with 95% confident level (the number of samples=280 for each confident interval).

Figure 2. Scatter plots for precipitation in (a) CTL and (b) ANO run (Wm^{-2}) with regression line in prescribed-SST simulation. The left and right columns show the data in DJF (wet season), JA (dry season), and annual mean (all season). The number of samples=280 for each scatter plot.

Figure 3. Classification of CTL MSE (J kg^{-1}) profiles by quartile of annual-mean ANO precipitation in prescribed-SST simulation. The values in legend are magnitude of group-mean ANO precipitation, confident interval of group-mean, and the sample size. Shaded area represents confident interval for every groups with 95% confident level (the number of samples=70 for red group and 69 for blue group). The dot and triangle signs in the left indicate the vertical levels where blue group significantly larger than red group (one-tailed t-test) with 90% and 95% confident level, respectively.

Figure 4. Annual-mean vertical MSE advection ($\text{J kg}^{-1} \text{ s}^{-1}$) in (a) CTL and (b) ANO in prescribed-SST simulation. The three figures below illustrate the MSE



profiles of three different contributors to ANO (thermodynamic effect, dynamic effect, and non-linear effect). Two lines in each subplot are classification result by quartile of annual-mean ANO precipitation. Shaded area represents confident interval with 95% confident level. The number of samples in the two groups is as the caption of Figure 3.

Figure 5. Annual-mean vertical advection of the two components of MSE ($\text{J kg}^{-1} \text{ s}^{-1}$), (a)

DSE ($CpT + gz$) and (b) moisture term ($Lvqv$) in prescribed-SST simulation.

Two lines in each subplot are classification result by quartile of annual-mean ANO precipitation. Shaded area represents confident interval with 95% confident level. The number of samples in the two groups is as the caption of Figure 3.

Figure 6. Annual-mean horizontal MSE advection ($\text{J kg}^{-1} \text{ s}^{-1}$) in (a) CTL and (b) ANO in

prescribed-SST simulation. The three figures below illustrate the MSE profiles of three different contributors to ANO (thermodynamic effect, dynamic effect, and non-linear effect). Two lines in each subplot are classification result by quartile of annual-mean ANO precipitation. Shaded area represents confident interval with 95% confident level. The number of samples in the two groups is as the caption of Figure 3.

Figure 7. Annual-mean horizontal advection of the two components of MSE ($\text{J kg}^{-1} \text{ s}^{-1}$),

(a) DSE ($CpT + gz$) and (b) moisture term ($Lvqv$) in prescribed-SST simulation. Two lines in each subplot are classification result by quartile of annual-mean ANO precipitation. Shaded area represents confident interval with 95% confident level. The number of samples in the two groups is as the caption of Figure 3.

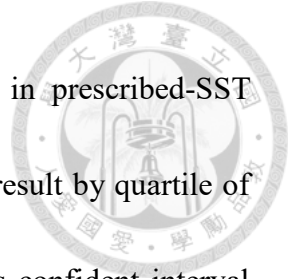



Figure 8. Annual-mean convergence of horizontal wind field (s^{-1}) profiles for (a) CTL (unit: $10^{-5}s^{-1}$) and (b) ANO (unit: $10^{-6}s^{-1}$) in prescribed-SST simulation. Two lines in each subplot are classification result by quartile of annual-mean ANO precipitation. Shaded area represents confident interval with 95% confident level. The number of samples in the two groups is as the caption of Figure 3.

Figure 9. Annual-mean vertical wind velocity ($Pa s^{-1}$) profiles for (a) CTL and (b) ANO in prescribed-SST simulation. Two lines in each subplot are classification result by quartile of annual-mean ANO precipitation. Shaded area represents confident interval with 95% confident level. The number of samples in the two groups is as the caption of Figure 3.

Figure 10. Illustrations for local MSE transportation in two scenarios with different MSE-concavity and different ANO precipitation. Three vertical profiles shown in left side are CTL MSE profiles relative to climatological mean, ANO vertical velocity, and ANO horizontal MSE advection. The schematic diagram in right



side depicts local MSE transports. Brown and blue area indicate land region and offshore region, respectively. Blue arrows and green arrows represent horizontal MSE advection and vertical MSE advection. Positive horizontal MSE advection means the advection towards land region.

Figure 11. Classification of CTL MSE profiles by quartile of annual-mean ANO precipitation in fully-coupled simulation. The values in legend are magnitude of group-mean ANO precipitation, confident interval of group-mean, and the sample size. Shaded area represents confident interval with 95% confident level (the number of samples=10 for the two groups respectively). The dot and triangle signs in the left indicate the vertical levels where blue group significantly larger than red group (one-tailed t-test) with 90% and 95% confident level, respectively.

Figure 12. Vertical profiles of empirical orthogonal functions (EOF) and time series of principal components (PC) for analysis of annual-mean CTL MSE profiles $hm\Delta$. The unit of EOF is $J kg^{-1}$.

LIST OF TABLES

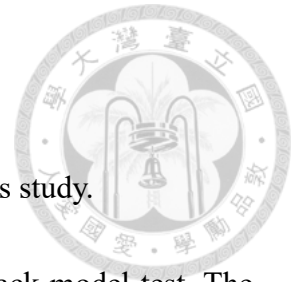


Table 1. Comparison of two global climate model experiments in this study.

Table 2. The climate responses of deforestation in the ocean feedback model test. The

magnitudes listed below are the spatial-average in the land region in the

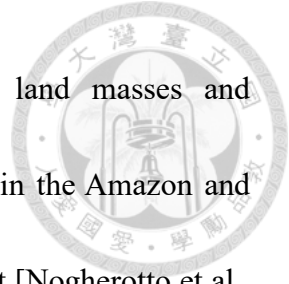
Maritime Continent. Asterisks represent the values that pass the significance

test.

Chapter 1 Introduction




Deforestation can influence regional climate states, including precipitation, surface energy, and the atmospheric circulation field [Nobre et al., 1991; Dickinson and Kennedy, 1992; Dirmeyer and Shukla, 1994; Polcher and Laval, 1994; Pielke et al., 2007; Chen et al., 2019; Chen and Dirmeyer, 2020; Lawrence et al., 2022]. Deforestation can redistribute the proportion of surface heat flux by decreasing the magnitude of latent heat flux, which causes more energy to be transmitted to the atmosphere in the form of sensible heat flux [Chen et al., 2019]. Higher sensible heat flux can result in higher lower-troposphere temperature, resulting in anomalous upward wind velocity [Chen et al., 2019]. In addition, low cloud cover decreases due to less latent heat flux and near-surface water vapor [Chen et al., 2019]; however, anomalous moist flux convergence from offshore regions induced by increasing the surface temperature can bring the moisture to compensate for the reducing moisture near the surface after deforestation [Henderson-sellers et al., 1993; McGuffie et al., 1995; Chen et al., 2019]. However, precipitation responses are dependent on changes in surface temperature and regional circulation patterns [de Oliveira et al., 2018]. Removing forests within the Maritime Continent could lead to higher mean precipitation in the long term (decadal time-scale) [Lawrence and Vandecar, 2015; Chen et al., 2019]. It's worth noting that low-level lateral moisture flux convergence would be crucial for bringing anomalous moisture to land regions in the



Maritime Continent after deforestation due to the fragmented land masses and surrounding oceans. On the other hand, this mechanism is weaker in the Amazon and Africa, where the effect of reduced evapotranspiration is more robust [Nogherotto et al., 2013; Lejeune et al., 2015].

In addition, the climate state in the Maritime Continent can be significantly affected by the El Niño–Southern Oscillation (ENSO), the main climate mode in the tropical Pacific region [Mcbride et al., 2003; Chang et al., 2004]. The magnitude of the Walker circulation in the El Niño phase would be weakened, leading to anomalous subsidence in the Maritime Continent and heralding an environment with high solar radiation, low atmospheric instability, and low cloud cover. In this kind of atmospheric environment, the deforestation responses can be strengthened, such as increases in long-term mean precipitation and surface temperature [Tölle et al., 2017; Lee and Lo, 2021]. In a simulation with high temporal resolution, deforestation would lead to higher maximum daily precipitation in El Niño cases [Tölle et al., 2017]. In addition, the idealized simulation for Maritime Continent deforestation under an El Niño condition, deforestation increased precipitation was amplified compared to the response under a neutral condition [Lee and Lo, 2021]. This discrepancy can be attributed to the different energy balances under these two states (El Niño vs La Niña) of large-scale circulation.

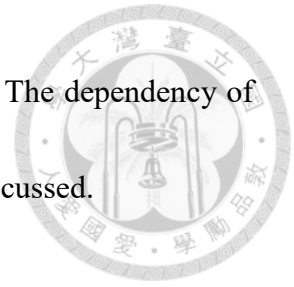
Such mean-state-dependent responses have been shown previously. For example,



global warming can lead to a stronger hydrological cycle and cause the wet season to become wetter in most rainy regions [Chou and Lan, 2012; Chou et al., 2013]. Furthermore, the changes in convective precipitation induced by global warming were dominated by the dynamic field structure in current mean-states [Liu et al., 2018]. In another study of global climate model, it was pointed out that more shallow convections and intense low-level upward motion can cause stronger moist static energy (MSE) convergence, thereby establishing an unstable environment under warming conditions [Chen et al., 2016]. These differences in the mean-states of convection environment and dynamic field can initiate different MSE transport patterns and gross moist stability [Neelin and Held, 1987]. In other words, the atmospheric environment can affect the responses of exogenous forcings, such as the land-use change effects on Indian climate under different sea surface temperature (SST) forcings [Halder et al., 2016] and the dependency of background wind speed and aerosol–cloud interaction [Gettelman et al., 2016] mentioned in some past studies.

Therefore, we proposed a hypothesis that the effect of deforestation is determined not only by changes in land type but also by the climate mean-states. Even with the fixed effects of land-surface changes, different background conditions may cause differences in deforestation responses. We used the specific SST condition to construct a large-scale atmospheric environment in the global climate model to simulate the change in

precipitation patterns after deforestation in the Maritime Continent. The dependency of atmospheric mean-states on the deforestation responses would be discussed.



Chapter 2 Data and Methodology

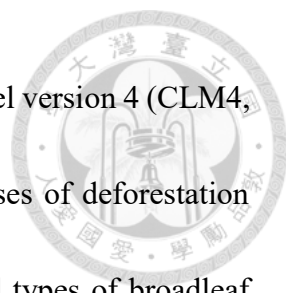


2.1 Model Experiments

We investigated the response to deforestation by using two groups of global climate model simulations: the CTL group, with the default configuration in land type, and the deforestation run (DEF) group, representing land surface conditions after deforestation. The differences between CTL and DEF (DEF minus CTL) were considered ANO and to reflect the net effect of deforestation. In the following sections, \bar{X} and X' represent the value of variables in CTL and ANO, respectively. We used the Community Earth System Model (CESM) to perform simulations with a horizontal spatial resolution of $0.9^\circ \times 1.25^\circ$, 30 vertical layers, and monthly data frequency. The domain we used in the analysis included all grids between 90°E and 140°E as well as 10°S and 10°N , and only land grids were selected. In the analysis, we considered only the spatial average over all land grids (with the land fraction larger than 0.5) and ignored any spatial variability. To obtain a robust mechanism of deforestation responses, two simulations with different model configurations were conducted (a full comparison is presented in Table 1).

In the prescribed-SST simulation, HadOIBI historical sea surface temperature (SST), combining HadISST [Rayner et al., 2003] and NOAA OI [Reynolds et al., 2007], were used to represent historical climate conditions driven by the ocean in both CTL and DEF.

We use CESM1 to conduct the experiment and Community Atmosphere Model version 5



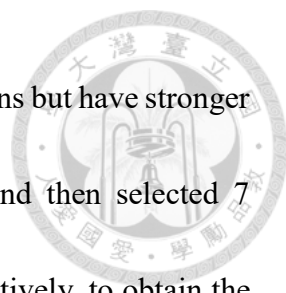
(CAM5, Neale et al., 2012) was coupled with Community Land Model version 4 (CLM4, Oleson et al., 2010; Lawrence et al., 2011) to represent the responses of deforestation considering the atmosphere-land interaction only. For DEF, all land types of broadleaf deciduous tropical trees and broadleaf evergreen tropical trees were replaced by grass.

In both CTL and DEF runs, 8 ensemble members were conducted with the same sea surface temperature (SST) and land type setting but slightly perturbed initial air temperature. Each ensemble member was spanned up from 1945 to 1969, and the data between July 1970 to June 2005 are used to be analyzed. Every year is started in July to match the evolution of ENSO so that the influence of ENSO on interannual variability can be clarified in subsequent. In the analysis of interannual variability, all 35 years in 8 ensemble simulations are treated as independent 280 samples.

We also conducted the simulation with a dynamic ocean to assess the differences between CTL and DEF. However, the same “year number” in CTL and DEF are not comparable in a long-term simulated fully-coupled run because they don’t have the same boundary condition to generate the same “mean-state”. To deal with it, we set a 1-year simulation for CTL and DEF experiments, and it’s expected that the climate mean-state during the year would be similar in both CTL and DEF due to the similar SST conditions. However, DEF configuration in the fully-coupled simulation is different from the prescribed-SST simulation because the effects of converting to C4 plants were too weak

to build up a deforest-like environment as prescribed-SST run. Therefore, the land type of tropical trees was replaced by bare soil, which contributes a very strong forcing to the water fluxes and energy fluxes to simulate the scenario of deforestation.

We selected several simulation starting points in the pre-industrial run carried out with CESM2. The 1-year deforestation experiment would be conducted starting from these starting points. The candidate events must spread in the different phases of climate oscillations to include most of the different climate states generated by climate natural variabilities. In this study, we selected 40 events from the pi-Control run based on Oceanic Niño Index (ONI), Pacific Decadal Oscillation (PDO), and Atlantic Multidecadal Oscillation (AMO). The phases of ENSO control the SST variation in the tropical Pacific Ocean, and the phases of PDO and AMO dominate the SST fluctuation in a multi-decadal timescale. These three climate oscillations are the first three principal components derived from the empirical orthogonal functions (EOF) of long-term global sea surface temperature (Messie and Chavez, 2011). We tried to capture the effects of these three modes that partially control the atmospheric mean-state interannually in the Maritime Continent. In addition, the indices must meet 3 conditions: (a) the standardized indices must be larger than 0.5 or less than -0.5 to ensure the impact of climate oscillation is strong enough to change the atmospheric mean-state, (b) the magnitude of indices of PDO and AMO must have the same sign with their 10-year running average to exclude some



sudden SST anomalies, (c) the years do not satisfy above two conditions but have stronger ONI values. We selected 26 events by the first two conditions and then selected 7 strongest El Niño and La Niña years with most extreme ONI, respectively, to obtain the other 14 events by the third condition. In the following analysis, we focused on the responses after deforestation in these 40 events, in which we can explore the role of different climate mean-states on the effect of land-use change forcings.

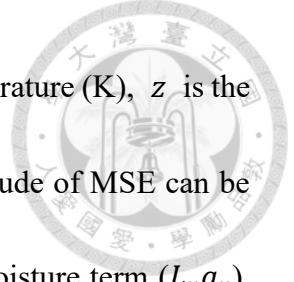
In both the prescribed-SST and the fully-coupled configurations, the ensemble simulations were conducted to eliminate the influence of internal variabilities. For the prescribed-SST simulation, the small perturbation in the atmospheric temperature, which is called “micro-perturbation”, was given to account for the uncertainties within the climate model. On the other hand, the cases in the fully-coupled simulation selected from different climatological oscillation phases were also a type of ensemble, which is called “macro-perturbation”. Both of these two methods of perturbing were intended to create different climate initial conditions.

2.2 Analysis of Moist Static Energy (MSE)

Moist static energy (MSE, or h_m , J kg⁻¹) is usually used to represent atmosphere energy including internal energy, gravitational energy, and latent heat of water:

$$h_m = C_p T + gz + L_v q_v \quad (1)$$

C_p is isobaric specific heat capacity (J kg⁻¹ K⁻¹), g is Gravitational acceleration (m



s^{-2}), and L_v is the latent heat of vaporization ($J\ kg^{-1}$). T is the temperature (K), z is the geopotential height (m), and q_v is the specific humidity. The magnitude of MSE can be decomposed into the dry static energy (DSE, $C_p T + gz$) and the moisture term ($L_v q_v$).

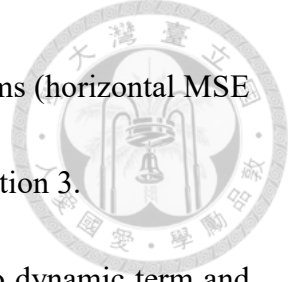
The vertical gradient of MSE stands for the thermodynamic instability of the atmosphere, so MSE vertical profile was calculated to indicate the overall environment related to convection motion and precipitation. In the following sections, MSE vertical profiles in CTL ($\overline{h_m} + \overline{h_{m\Delta}}$) will be shown as an anomaly ($\overline{h_{m\Delta}}$) to climatological mean ($\overline{h_m}$), so does in ANO ($h'_m + h'_{m\Delta}$). The sign \overline{X} denotes the values in CTL and X' denotes the values in ANO.

To analyze the MSE change between CTL and DEF, we decompose the change in MSE in every single layer into different terms in the following context (Zheng et al., 2020):

$$\frac{dh_m}{dt} = -\vec{V} \cdot \nabla h_m - \omega \frac{\partial h_m}{\partial p} + F_{net} + \varepsilon \quad (2)$$

Each term represents different components in the MSE budget: local change in MSE, horizontal advection, vertical advection, net heat source, and residual. \vec{V} is the horizontal wind field, ω is the vertical wind velocity, and residual term (ε , including sub-gridded transport which cannot be resolved in the model, error from time mean or model numerical calculation). F_{net} is comprised of all heat sources including radiative heating rate (Q_R), latent heat flux (LH), and sensible heat flux (SH).

We clarify the primary role of the atmospheric energy transfer from the MSE budget



analysis by exploring the vertical profile changes of the first two terms (horizontal MSE advection and vertical MSE advection) of the right-hand side in equation 3.

In ANO, change in MSE advection term can be decomposed into dynamic term and thermodynamic term:

$$(-\vec{V} \cdot \nabla h_m)' = -\vec{V}' \cdot \nabla \bar{h}_m - \vec{V} \cdot \nabla h_m' - \vec{V}' \cdot \nabla h_m' \quad (3)$$

$$\left(-\omega \frac{\partial h_m}{\partial p}\right)' = -\omega' \frac{\partial \bar{h}_m}{\partial p} - \bar{\omega} \frac{\partial h_m'}{\partial p} - \omega' \frac{\partial h_m'}{\partial p} \quad (4)$$

In the end, we would depict a pattern of local transport of MSE advection, which consists of vertical MSE advection and horizontal MSE advection between the land region and adjacent offshore region. We will compare the transport among different classified groups and find out its correlation with the increases in ANO precipitation.

2.3 Grouping of Events

We tried to figure out the relation between MSE profile characteristics in CTL and precipitation in ANO (that is, the deforestation-induced response in precipitation). To capture the certain feature of all mean-states and their response in ANO precipitation, we selected the events into two groups based on the quartiles by corresponding ANO precipitation, that is, the events that have “greater magnitude” and “smaller magnitude” of precipitation increases., respectively. The events with ANO precipitation below the 1st quartile and above 3th quartile were selected into these two groups. The remaining events (within the 1st to the 3th quartile of ANO precipitation) would be considered neutral

conditions and would not be analyzed. In the following analysis, we discuss the discrepancies in climate conditions in these two groups and conclude the mechanism associated with the different deforestation-induced responses.



2.4 Tests of Significance

All the confident intervals in the vertical profiles and seasonal cycle diagrams were calculated by $\bar{X} \pm t_{0.025} s/\sqrt{n}$ to give an estimation of the mean values. $t_{0.025}$ is the critical value of the t distribution with a 95% confidence level (two-tailed test). In Figure 3 and Figure 11, the significance tests for the two groups is two-tailed Student's t-test that determines whether the magnitudes in each level of vertical profile in one group are larger than another group.

Chapter 3 Results


3.1 Patterns of Climatological Precipitation in the Maritime Continent



In the Maritime Continent, the wet season spans from September to April, with the other months typically considered the dry season (Figure 1a). After deforestation, precipitation is significantly higher in all seasons (Figure 1b), but with no significant between-season differences. There is only a slightly greater precipitation increase in the dry season. On the other hand, annual mean precipitation in the anomalies (ANO) is significantly negatively correlated with that in the control run (CTL; Figure 2a). In other words, the responses to deforestation tend to provide a negative-feedback effect on interannual scales, demonstrating a “dry-get-wetter” pattern in the variability in the precipitation. In comparison, the responses to the global warming forcing have “wet-gets-wetter” patterns on spatial or seasonal scales as shown in previous studies [Chen et al., 2016]. Based on the negative correlation, we can conclude that the climate mean-state with lower precipitation in CTL tends to have higher precipitation after deforestation at the interannual scale.

3.2 Characteristic of MSE Mean-states

Figure 3 illustrates the grouping profiles of CTL MSE $\overline{h_{m\Delta}}$ and the values listed in the legend are sorted by magnitudes of group-mean ANO precipitation. The two groups




with the greatest and smallest ANO precipitation have negative and positive MSE anomalies in the middle troposphere, respectively. In contrast, the interannual variability of MSE is less divergent in the lower and upper troposphere. For the significance of the difference between the two groups, the confidence intervals of the two lines can be considered as the discrepancy between every case within the group. According to the test of the significance of the difference, it can be known that the difference in the magnitude of MSE in the middle troposphere is the most significant.

Based on the result of grouping, we can conclude that anomalous magnitudes of MSE in the middle troposphere and ANO precipitation have some relation. In the events that ANO precipitation is greater or less than the climatological mean, corresponding MSE profiles have “negative-concave” and “positive-concave” characteristics. The shape of the MSE profile affects the vertical thermodynamic structure and atmospheric instability. In negative-concave cases, MSE has a negative gradient (unstable environment) in the lower troposphere, and such a long-term environment might be more conducive to the occurrence of convective motion.

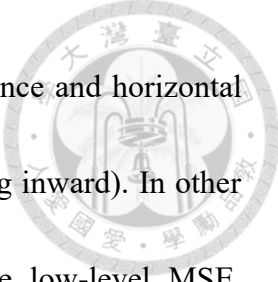
3.3 Role of MSE Budget

In CTL, there is a positive upwards vertical advection of MSE from the surface to 700 hPa and a negative upwards vertical advection above 700 hPa (Figure 4a). The direction of vertical MSE transport is dominated by the gradient of the typical profile of MSE in



tropical climatological mean. Based on the results of quartile grouping, the group which has greater ANO precipitation has weaker MSE advection in CTL. After deforestation, magnitudes of upward vertical MSE advection are enhanced (Figure 4b). The groups with greater ANO precipitation show significantly stronger increases in vertical transport. Moreover, change in the vertical velocity (so-called dynamic term) mainly accounts for enhanced MSE vertical transport (Figure 4c). On the other hand, change in the MSE profile (thermodynamic term) has an opposite effect from the surface to 700 hPa (Figure 4d), but the values are one order of magnitude less than the dynamic term. In the group with the smallest ANO precipitation, the thermodynamic term contributes to upward MSE advection between 850 hPa to 700 hPa, which can be attributed to the positive gradient of MSE in ANO above 850 hPa. Besides, non-linear terms have similar magnitudes, leading to upward transport from nearly 700 hPa to 600 hPa (Figure 4e). From the perspective of the two parts of MSE, the vertical advection is dominated by the moisture term, while the vertical advection of DSE has an opposite contribution (Figure 5). The negative contribution of DSE on the enhanced vertical advection of MSE has a consistent magnitude above 800 hPa, and the positive effect of the moisture term can be roughly offset in the upper troposphere.

The horizontal advection of MSE in CTL is negative from the surface to the middle troposphere (Figure 6a). This is caused by the gradient between the land region and the



adjacent sea region (Figure 8b, the signs of horizontal wind divergence and horizontal advection are opposite, implying that the gradient of MSE is pointing inward). In other words, horizontal convergence has a negative contribution to the low-level MSE. Deforestation leads to an anomalous MSE convergence near the surface, and a divergence above 900 hPa (Figure 6b). Deforestation leads to weaker latent heat fluxes at the surface, and MSE near the surface will decrease, intensifying the gradient between land and offshore region. Depending on the groups with different ANO precipitation, the anomalous divergence between 900 hPa to 600 hPa is weaker in the groups, which have greater ANO precipitation. In three components of ANO horizontal advection, change in MSE gradient (thermodynamic term) shows a similar pattern to total ANO horizontal advection (Figure 6d), while there is anomalous negative advection between 900 hPa to 700 hPa for the group with smaller ANO precipitation. Change in wind field (dynamic term) tends to strengthen positive MSE advection for all groups (Figure 6c). It is worth noting that the magnitude of non-linear terms (the correlation between wind field anomaly and MSE gradient anomaly) cannot be ignored, which brings in a consistent MSE divergence across almost the whole troposphere (Figure 6e). For horizontal MSE advection, the differences between the four groups are not clear as vertical MSE advection, except for the anomalous convergence in 850 hPa to 700 hPa.

The decomposition of the horizontal advection of MSE (Figure 7) implies that the

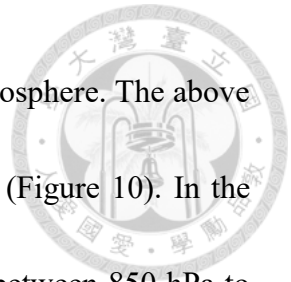
contribution of the moisture term is dominant. The conflicting effect of DSE partially offsets the enhanced horizontal advection of MSE below 900 hPa, but the magnitude decays with the height rapidly.



3.4 Local Transport of MSE

Based on the above analysis for MSE advection, we found that there's stronger negative horizontal advection between 850 hPa to 500 hPa for the group with smaller ANO precipitation (Figure 6b), and the upward vertical advection is much weaker than other groups (Figure 4a). On the other hand, the group with greater ANO precipitation shows weaker negative horizontal advection below 500 hPa, but there's negative horizontal advection in the upper troposphere (It is worth noting that the pattern of this "vertical discrepancy of the horizontal advection" can be found in the horizontal advection of the moisture term shown as Figure 7 shown). For vertical wind velocities, deforestation brings consistent upward anomalies for all groups (Figure 9b) compared to the original upward environment in CTL (Figure 9a), which implies a stronger local transport for MSE transport caused by deforestation for all characteristics of mean-states. From the wind field viewpoint, there's an anomalous convergence layer and an anomalous divergence layer near the surface after deforestation (Figure 8b) compared to the local wind field in CTL (Figure 8a). For the group with greater ANO precipitation, the convergence layer is thicker, and the divergence layer can extend to nearly 500 hPa.

Moreover, there's a stronger anomalous divergence in the upper troposphere. The above feature can be summarized as a different pattern of MSE transport (Figure 10). In the scenario that the magnitude of negative horizontal MSE advection between 850 hPa to 500 hPa is weaker, there's a deeper MSE transport extended to the upper troposphere, with stronger upward vertical MSE advection in the low troposphere and horizontal divergence in the upper troposphere. In addition, deeper MSE transport has a high correlation with greater precipitation increases after deforestation, and vice versa.





Chapter 4 Discussion

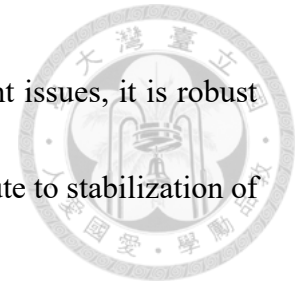
4.1 The Seasonality of Precipitation Responses

We found different levels of correlations between ANO precipitation and CTL precipitation (Figure 2). A stronger correlation between CTL precipitation and ANO precipitation is observed if only the wet season is included to calculate the interannual variation (Figure 2b). On the contrary, the CTL precipitation in the dry season (July–August) has a higher interannual variability and lower R^2 values (Figure 2c) than does the precipitation in the wet season (December–January–February).

4.2 Role of Ocean Feedback

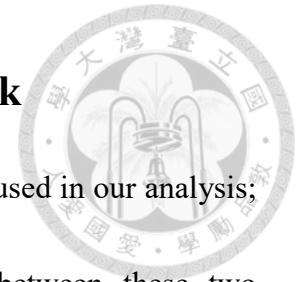
Deforestation leads to the alternation of the hydrological cycle and energy cycle, so the environments in both the land region and the adjacent offshore region are important to the responses in the Maritime Continent. Early studies showed that change in equatorial easterlies in Western Pacific would affect the strength of upwelling current, as well as SST and ocean evaporation fluxes. Delire (2001) compared deforestation experiments with fully-coupled (dynamic ocean) and fixed SST configurations and found that the weaker equatorial easterlies in the fully-coupled run. Therefore, precipitation over the Maritime Continent is greater in the fixed SST run compared to the fully-coupled run. However, Schneck and Mosbrugger (2011) obtained opposite results, which have stronger equatorial easterlies and less precipitation in the fully-coupled run. Although different

studies have found contrary conclusions due to the model-dependent issues, it is robust that stronger cooling effect caused by upwelling current can contribute to stabilization of the convective environment [Schneck and Mosbrugger, 2011].



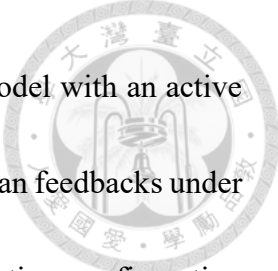
To evaluate the effects of ocean feedback in a global climate model, the relations between the CTL MSE profile and ANO precipitation simulated by fully-coupled simulations were discussed. Figure 11 illustrates the grouping profiles of CTL MSE $\overline{h_{m\Delta}}$ in fully-coupled simulations, grouped by ANO quartiles (as same as Figure 3). The groups with the greatest and smallest ANO precipitation have a negative-concave and positive-concave profile, respectively, which is the same as the result in the prescribed-SST simulation. According to the above discussion, we believe that the connection of CTL MSE and ANO precipitation is still robust under the condition of considering the dynamic ocean model. It's worth noting that, compared with those in the prescribed-SST simulations, the amplitudes of MSE profile concavity in the fully coupled simulations are larger. This may be attributable to the more extreme events in the fully coupled runs (selected from the 2000-year pi-Control simulation), and the stronger oscillation of MSE concavity can be created. In contrast, the oscillation of MSE profiles in the prescribed-SST simulation, which was induced by the 35-year historical SST forcings, has a smaller, more constrained annual variability in profile concavities.

4.3 Model Test for Long-term Ocean Feedback



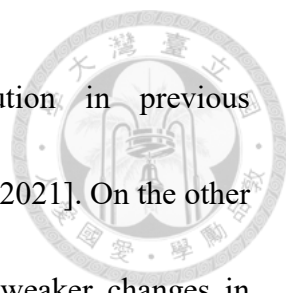
The fully-coupled and prescribed-SST climate model were both used in our analysis; however, the detailed differences to deforestation experiment between these two configurations still lack comparison. There're several discrepancies in these two experiments: (a) version of model (CESM1 & CESM2), (b) initial condition (present day & pi-Control), (c) simulated time length (long-term simulation & transient simulation), (d) deforested forcing (converting to C4 plant & converting to bare soil). Each difference of above factors is necessary to be disentangled to clarify the model performance on deforest-experiment. For example, how the forcings of deforestation were setup is critical in model experiment. It had been understood in our analysis that converting to C4 plant in 1-year fully-coupled run is not robust enough to build up typical responses as in prescribed-SST run. In the other word, it's worthy to notice that the effect of "C4 type deforestation" costs time to reach its steady-state while we try to conduct a transient deforest experiment analysis in fully-coupled climate model.

Differences in model versions and simulation time length might still cause uncertainties in the results. If we want to obtain the quantitative impact on deforestation responses from the dynamic ocean, more simulations with different experiment configurations must be operated to determine the effect of each factor (such as versions of parameterization, simulation time length, the initial conditions of land type and



aerosols) on the climate responses. Hence, a fully coupled climate model with an active ocean model test was conducted to compare the effect of including ocean feedbacks under the same initial states (pi-Control condition) and the same deforestation configuration (convert to bare soil), so the effect of ocean feedbacks could be isolated. The model test was conducted by Community Earth System Model version 2. The prescribed-SST run (PreOcean), slab-ocean run (SbOcean), and the fully-coupled run (CpOcean) were simulated for 30 years (last 25 years for analysis), 30 years (last 25 years for analysis), and 100 years (last 50 years for analysis), respectively. The long-term responses to deforestation were analyzed. In these three different configurations, the pre-industrial initial states were used. To ensure the consistency in the land surface condition, the initial surface dataset in fully-coupled simulations was replaced as same as the prescribed-SST. The results are listed in Table 2.

In the CpOcean run (coupled ocean), the climatological precipitation is greater, but the response of deforestation is smaller. This can be linked to the negative feedback relationship for interannual precipitation variability seen in Figure 2 in this study. Moreover, comparing to the PreOcean (prescribed-SST ocean) run, the climatological land surface temperature, climatological land Bowen ratio, and climatological offshore SST (not shown) are all significantly greater in the CpOcean run. Though, the systematic biases of SST and air-sea flux caused by coupling ocean model were found to have high




dependencies in model parameterizations and spatial resolution in previous coupled/uncoupled comparison studies [Xue et al., 2020; Fujii et al., 2021]. On the other hand, a weaker increase in precipitation might be related to the weaker changes in increasing sensible heat flux (SH) and decreasing latent heat flux (LH) in the fully-coupled run. This is similar to the phenomenon mentioned in the previous study that the magnitudes of SH&LH responses have a dependency on the climatological Bowen ratio [Chen and Lo, under review].

On the other hand, the SbOcean (slab ocean) run shows a different climatological state. Even the stronger climatological SH, LH, and hotter surface temperature can be found, the climatological precipitation is less than the PreOcean run. In the responses caused by deforestation, the increase of precipitation in the SbOcean run is weaker than the CpOcean run, but the increase in SH and the decrease in LH is more severe than the PreOcean run. All these facts mean that although the mechanism of the slab ocean can make the surface energy flux more responsive, there are other effects that inhibit the increase in precipitation except the SH&LH response. Therefore, the "precipitation increase" and the "SH&LH change" of the three runs (prescribed, slab, and fully-coupled ocean) did not completely show the same relationship.

4.4 Role of Vertical Wind Velocities

In CTL, MSE profiles can be used to determine the atmosphere instability of the mean-




states. For the group with a negative-concave MSE profile, there's an anomalous positive MSE gradient in the low troposphere, and this leads to greater convective instability. However, convective precipitation is not only determined by thermodynamic instability; vertical velocity is also related to the strength of convective motion. Deforestation-induced anomalous upward MSE vertical advection is strengthened below 700 hPa in the group with greater ANO precipitation (Figure 4b), which can be attributed to changes in the gradient of the MSE profile and upward vertical velocity anomaly. Furthermore, the dynamic term of MSE vertical advection ($-\omega' \partial \overline{h_m} / \partial p$) is more positive for the group with greater ANO precipitation between the surface to 700 hPa (Figure 4c). For negative-concave groups, the magnitude of advection depends on the positive effect from stronger anomalous vertical velocity and more positive $\partial \overline{h_m} / \partial p$; the response of ultimate advection cannot be simply attributed to one of the factors. Based on the above examples, the co-exist of stronger upward ANO vertical velocity and greater positive gradient of CTL MSE is more important than the separate effects of the two factors, leading to enhanced ANO MSE vertical advection among the four groups. The characteristic of the MSE profile has a high correlation to the pattern of vertical velocity, but the causality between the two factors deserves future work.

4.5 The Contributors to the Interannual Variabilities of

MSE Profiles



Empirical orthogonal function (EOF) analysis is used to decompose data and extract the main component that explains the largest variability by a series of orthogonal functions. For prescribed-SST simulations, the first two principal components (PC1, PC2) of CTL MSE profiles $\overline{h_{m\Delta}}$ over the whole troposphere represent long-term warming trend and ENSO mode, respectively (Figure 12). EOF 1 shows uniform positive values in the MSE profile. With the increasing trend of PC1, mode 1 of EOF stands for a consistent warming trend for MSE over the whole troposphere. However, warming rates in different parts of the troposphere are uneven. The uneven warming might cause long-term changes in CTL MSE profile pattern, but the relationship between this change in environment and the response of deforestation have not been clarified here. On the other hand, EOF 2 shows a negative value in the middle atmosphere. The interannual variability with negative-concave and positive-concave patterns can be generated through the oscillation of PC2. Mode 2 of EOF is mainly dominated by large-scale oscillation, especially ENSO. The correlation coefficients between PC2 and annual-mean Ocean Niño Index (ONI) are 0.70 (the figures were not listed here). The several main positive (negative) peaks in the PC time series can correspond to historical El Niño (La Niña) events. From the results of EOF2, ENSO has a large impact on the characteristic of the MSE profile in a multi-year oscillation period. The relationship between concave-type



and ENSO also provides an explanation that the negative-concave group has a stronger magnitude of MSE anomaly. In historical observation, the extreme El Niño has a higher frequency than the extreme La Niña [Trenberth, 1997]. More extreme El Niño events might contribute to the negative-concave group and lead to an asymmetric MSE profile with “stronger” negative-concave and “weaker” positive-concave.

4.6 Features of Simulation using Global Climate Model

Although global climate models’ spatial resolution is coarse, such experiment tools can take into account the responses of the global climate system, hydrological cycle, and biogeochemical processes more broadly. In contrast, mesoscale numerical weather simulation can resolve regional characteristics better, including land-surface state and topography effects, but the interaction between the region and the large-scale environment may not be considered. In addition, in this study, the SST pattern in global climate models is the key to controlling the global atmospheric climate state. In future studies, more alternatives could be utilized to simulate the climate response, such as the atmospheric nudging approach in the global model simulations [Chen et al., 2021].

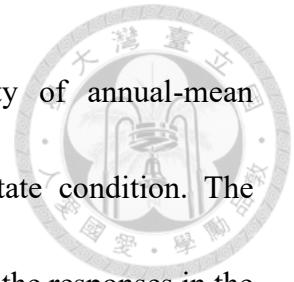
Chapter 5 Conclusion



This study clarifies the relationship between the responses of deforestation in the MC land regions and its local climate mean-state, primarily determined by the natural variabilities in the climate system. Analyses from prescribed-SST and fully-coupled simulations indicate that the drier mean-state environment can have a stronger increase in precipitation after deforestation, also altering the interannual variability of land precipitation in the Maritime Continent. The MSE mean-state with a negative-concave profile type is prone to induce greater increases in precipitation after deforestation. Based on the analysis of the MSE budget, we speculated that the stronger MSE vertical advection in the lower troposphere and stronger negative MSE horizontal advection between 900 hPa to 600 hPa, which jointly build up a deeper MSE local transport that induces more energy into the terrestrial region in the Maritime Continent. The gradient of the negative-concave MSE profile in the lower troposphere provides a more unstable environment, favorable to stronger upward motion and enhanced local transport, leading to greater annual-mean precipitation after deforestation.

This study implies that although the same magnitude of the forcings is given in the experiment, the local responses can be distinguished due to different background atmospheric environments caused by natural climate variabilities. Changes in precipitation between the control and deforestation run also reveal a negative feedback,

in which deforestation can modulate the interannual variability of annual-mean precipitation by bringing greater precipitation in a drier mean-state condition. The mechanism proposed in this study can help understand and diagnose the responses in the Earth system caused by external anthropogenic forcings (such as the greenhouse gases) in consideration of different mean-states (namely the internal variability in the Earth system).



FIGURES

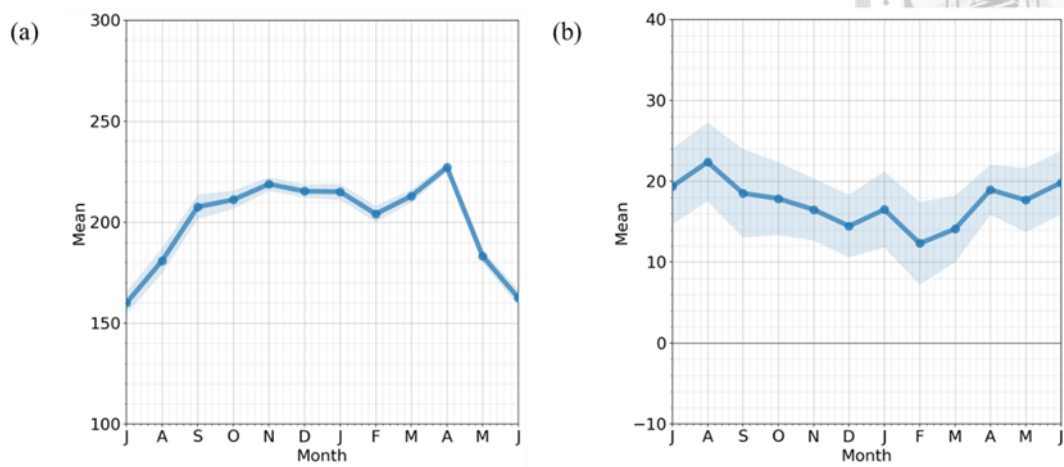


Figure 1. Seasonal cycle of precipitation in (a) CTL and (b) ANO run (Wm^{-2}) in prescribed-SST simulation. Horizontal axis is month and starts from July to June next year. Shaded area represents confident interval with 95% confident level (the number of samples=280 for each confident interval).

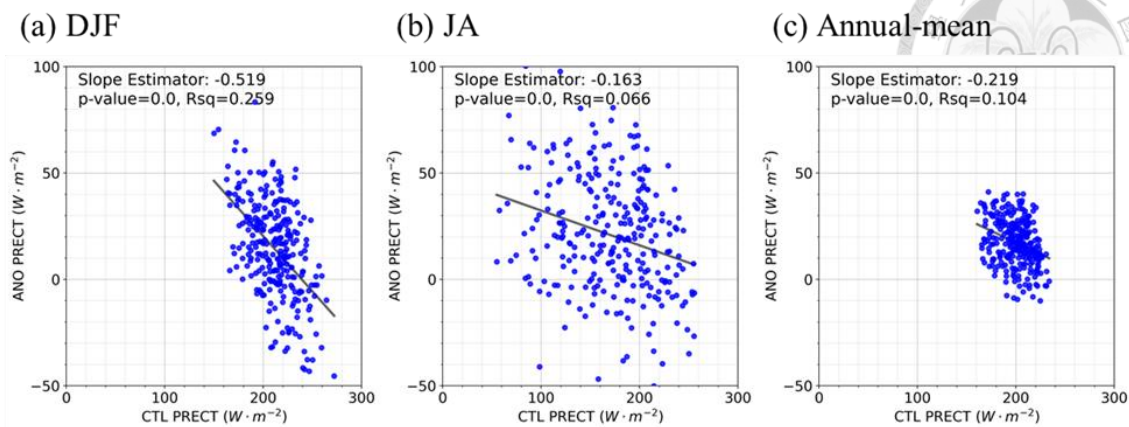


Figure 2. Scatter plots for precipitation in (a) CTL and (b) ANO run (Wm^{-2}) with regression line in prescribed-SST simulation. The left and right columns show the data in DJF (wet season), JA (dry season), and annual mean (all season). The number of samples=280 for each scatter plot.

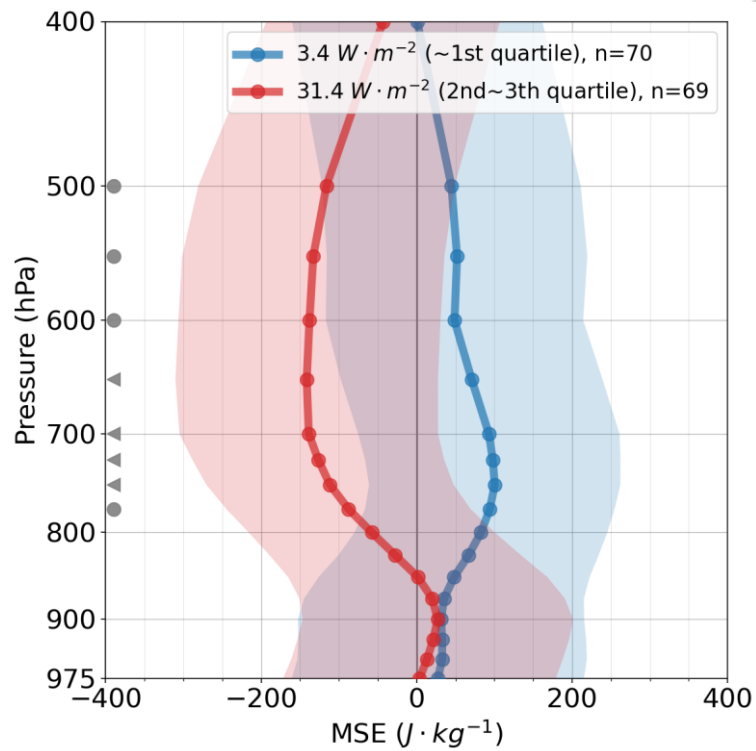


Figure 3. Classification of CTL MSE ($J \cdot kg^{-1}$) profiles by quartile of annual-mean ANO precipitation in prescribed-SST simulation. The values in legend are magnitude of group-mean ANO precipitation, confident interval of group-mean, and the sample size. Shaded area represents confident interval for every groups with 95% confident level (the number of samples=70 for red group and 69 for blue group). The dot and triangle signs in the left indicate the vertical levels where blue group significantly larger than red group (one-tailed t-test) with 90% and 95% confident level, respectively.

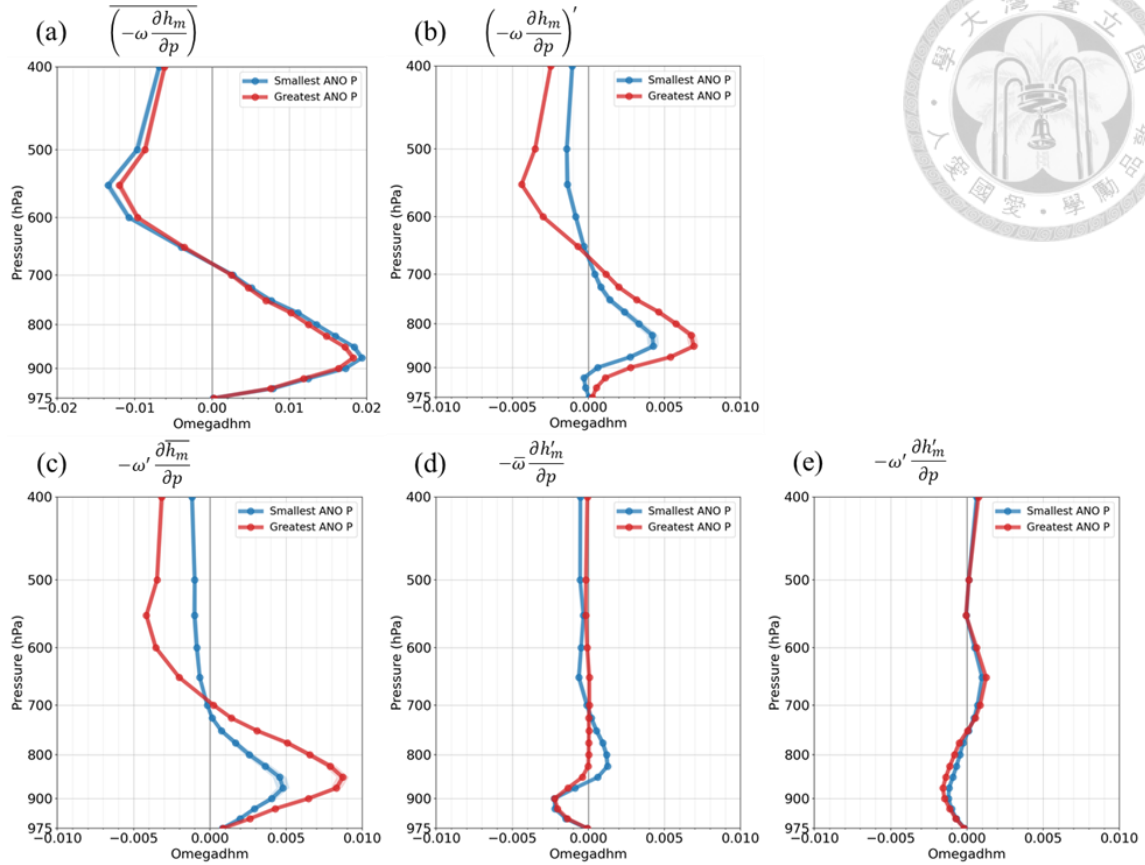


Figure 4. Annual-mean vertical MSE advection ($\text{J kg}^{-1} \text{s}^{-1}$) in (a) CTL and (b) ANO in prescribed-SST simulation. The three figures below illustrate the MSE profiles of three different contributors to ANO (thermodynamic effect, dynamic effect, and non-linear effect). Two lines in each subplot are classification result by quartile of annual-mean ANO precipitation. Shaded area represents confident interval with 95% confident level. The number of samples in the two groups is as the caption of Figure 3.

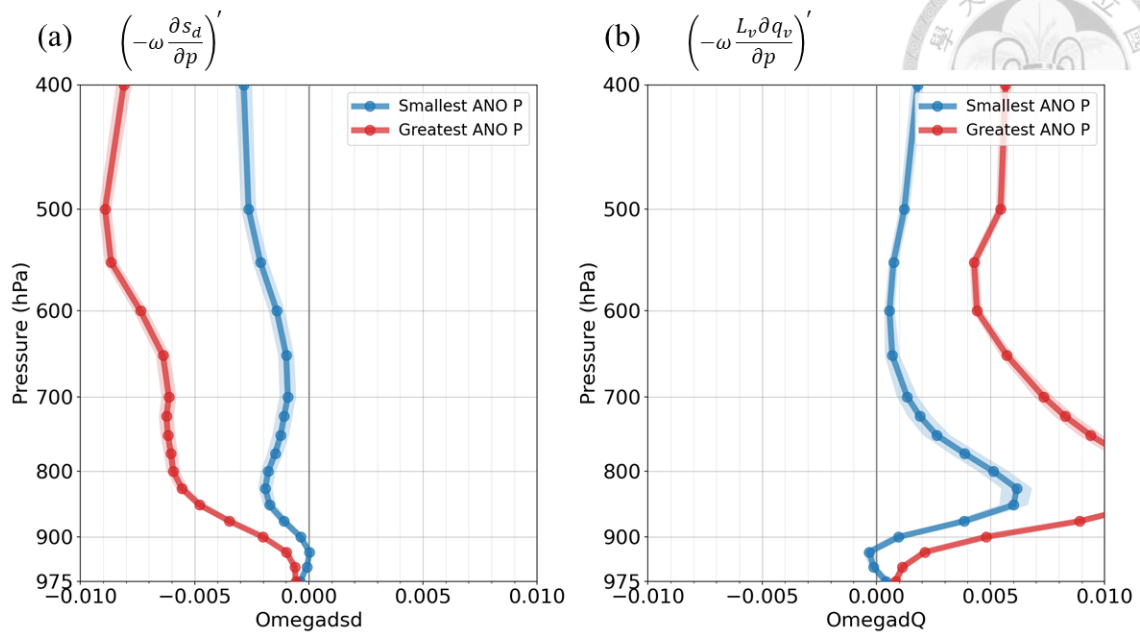


Figure 5. Annual-mean vertical advection of the two components of MSE ($\text{J kg}^{-1} \text{s}^{-1}$), (a) DSE ($C_p T + gz$) and (b) moisture term ($L_v q_v$) in prescribed-SST simulation. Two lines in each subplot are classification result by quartile of annual-mean ANO precipitation. Shaded area represents confident interval with 95% confident level. The number of samples in the two groups is as the caption of Figure 3.

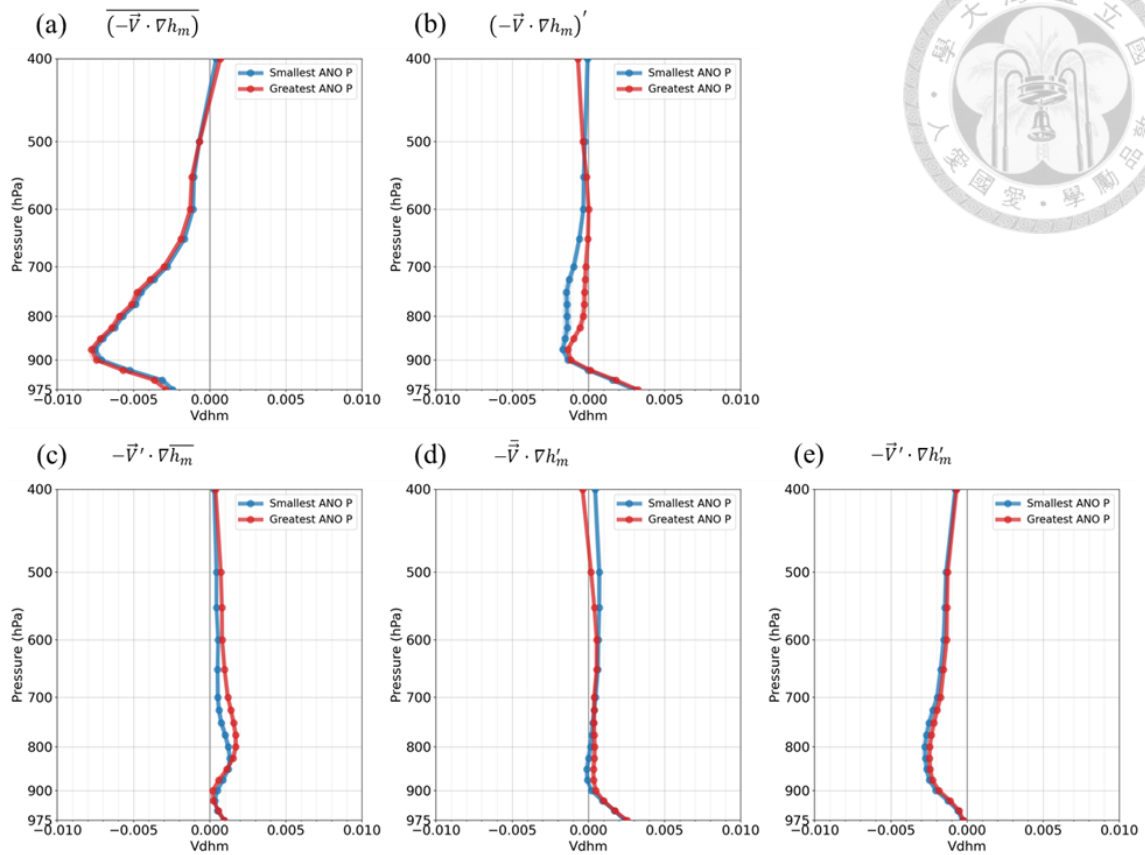


Figure 6. Annual-mean horizontal MSE advection ($\text{J kg}^{-1} \text{s}^{-1}$) in (a) CTL and (b) ANO in prescribed-SST simulation. The three figures below illustrate the MSE profiles of three different contributors to ANO (thermodynamic effect, dynamic effect, and non-linear effect). Two lines in each subplot are classification result by quartile of annual-mean ANO precipitation. Shaded area represents confident interval with 95% confident level. The number of samples in the two groups is as the caption of Figure 3.

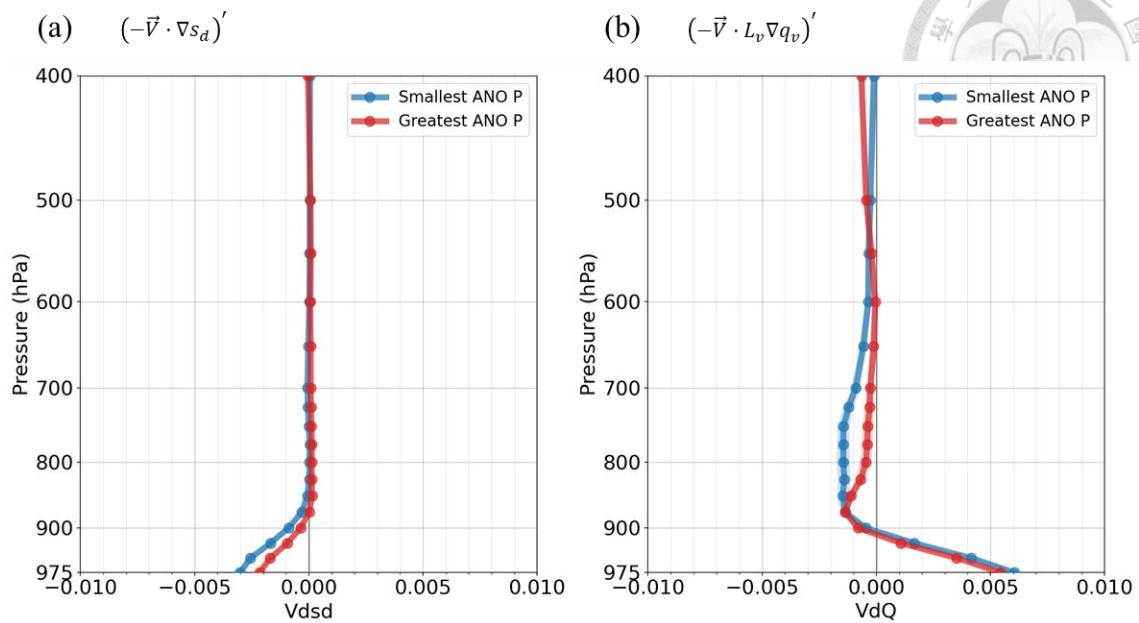


Figure 7. Annual-mean horizontal advection of the two components of MSE ($\text{J kg}^{-1} \text{s}^{-1}$), (a) DSE ($C_p T + gz$) and (b) moisture term ($L_v q_v$) in prescribed-SST simulation. Two lines in each subplot are classification result by quartile of annual-mean ANO precipitation. Shaded area represents confident interval with 95% confident level. The number of samples in the two groups is as the caption of Figure 3.

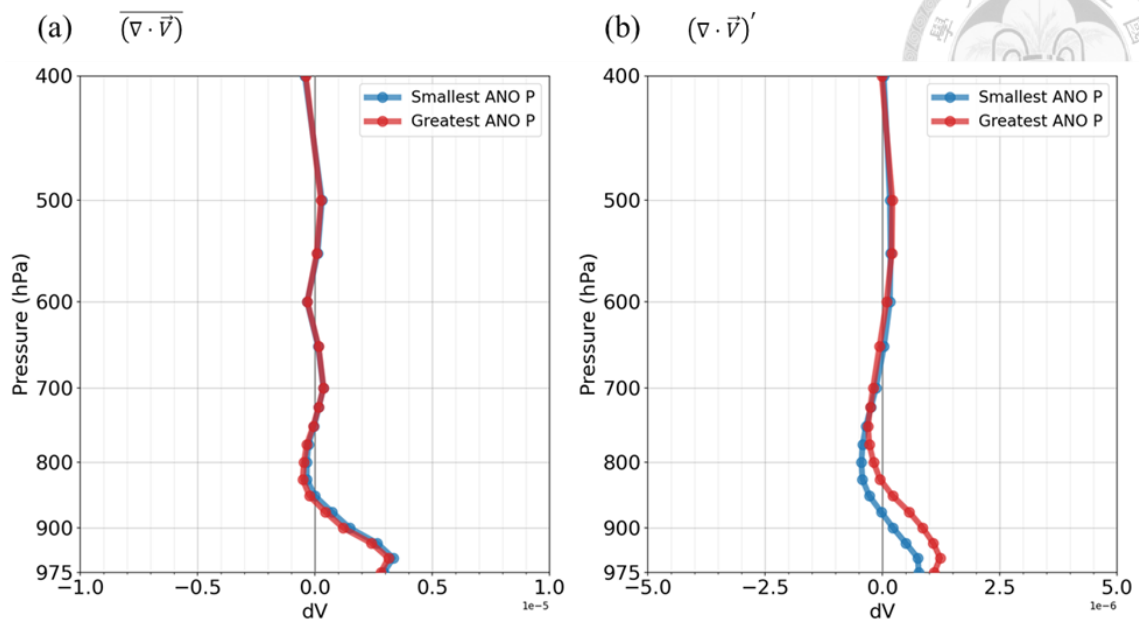


Figure 8. Annual-mean convergence of horizontal wind field (s^{-1}) profiles for (a) CTL (unit: 10^{-5}s^{-1}) and (b) ANO (unit: 10^{-6}s^{-1}) in prescribed-SST simulation. Two lines in each subplot are classification result by quartile of annual-mean ANO precipitation. Shaded area represents confident interval with 95% confident level. The number of samples in the two groups is as the caption of Figure 3.

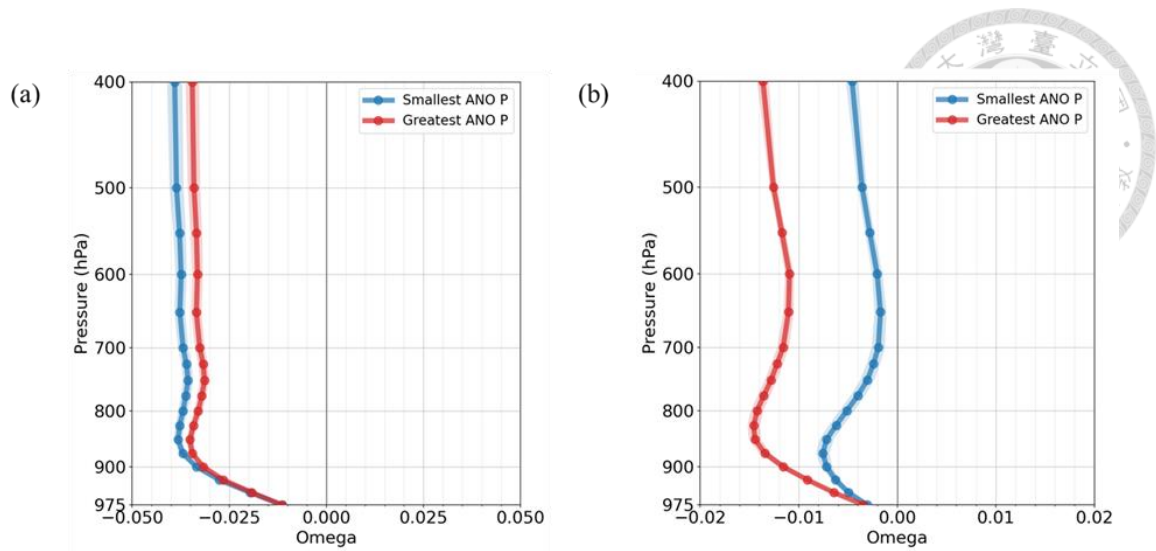
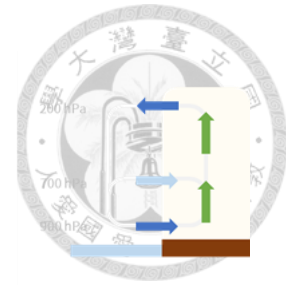
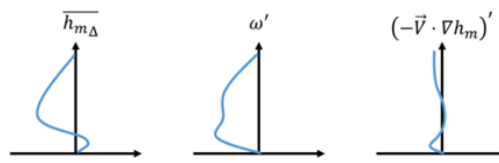


Figure 9. Annual-mean vertical wind velocity (Pa s^{-1}) profiles for (a) CTL and (b) ANO in prescribed-SST simulation. Two lines in each subplot are classification result by quartile of annual-mean ANO precipitation. Shaded area represents confident interval with 95% confident level. The number of samples in the two groups is as the caption of Figure 3.

Negative-concave Profile
 Greater ANO Precipitation



Positive-concave Profile
 Smaller ANO Precipitation

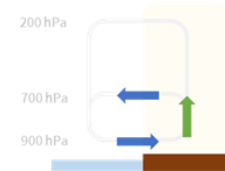
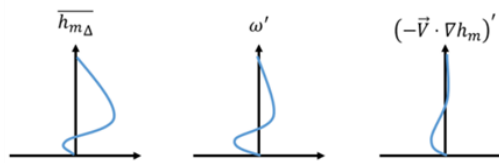


Figure 10. Illustrations for local MSE transportation in two scenarios with different MSE-concavity and different ANO precipitation. Three vertical profiles shown in left side are CTL MSE profiles relative to climatological mean, ANO vertical velocity, and ANO horizontal MSE advection. The schematic diagram in right side depicts local MSE transports. Brown and blue area indicate land region and offshore region, respectively. Blue arrows and green arrows represent horizontal MSE advection and vertical MSE advection. Positive horizontal MSE advection means the advection towards land region.

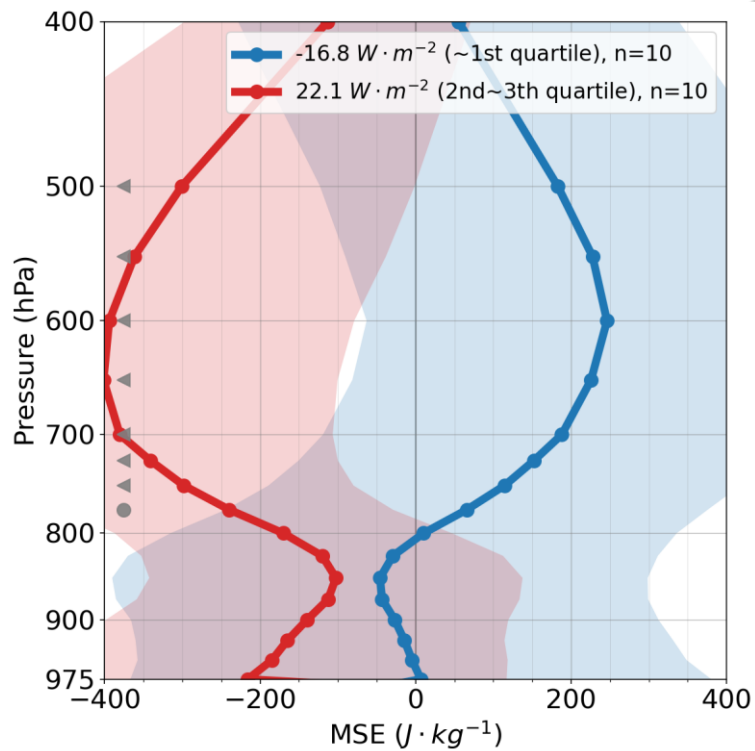


Figure 11. Classification of CTL MSE profiles by quartile of annual-mean ANO precipitation in fully-coupled simulation. The values in legend are magnitude of group-mean ANO precipitation, confident interval of group-mean, and the sample size. Shaded area represents confident interval with 95% confident level (the number of samples=10 for the two groups respectively). The dot and triangle signs in the left indicate the vertical levels where blue group significantly larger than red group (one-tailed t-test) with 90% and 95% confident level, respectively.

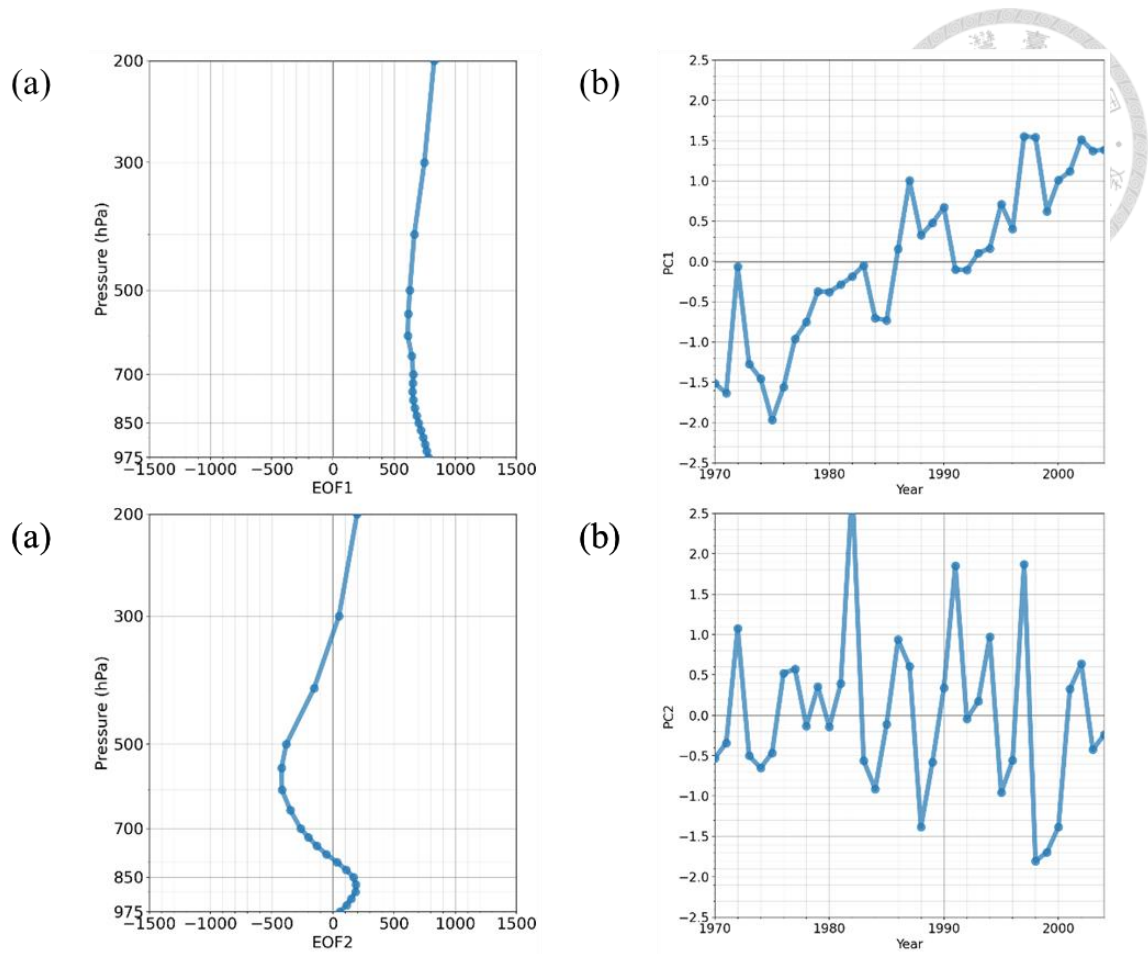


Figure 12. Vertical profiles of empirical orthogonal functions (EOF) and time series of principal components (PC) for analysis of annual-mean CTL MSE profiles $\overline{h_{m\Delta}}$. The unit of EOF is J kg^{-1} .

TABLES

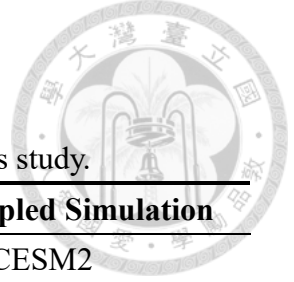


Table 1. Comparison of two global climate model experiments in this study.

	Prescribed-SST Simulation	Fully-coupled Simulation
Model Version	CESM1	CESM2
Model component set and initial states	Present-day	Pre-industrial control
Atmosphere	Simulated, CAM5	Simulated, CAM6
Land	Simulated, CLM4	Simulated, CLM5 BGC
Deforest-Experiment	Tropical tree to C4	Tropical tree to bare soil
Ocean	Prescribed, HadOIBI SST	Simulated, POP2
Spatial resolution	0.9°x1.25°	
Vertical resolution	30 layers	
Data frequency	Monthly	
Ensemble	8 members (Micro-perturbation)	26 members (Macro-perturbation)
Spin-up years	1945 to 1969, 25 years	Jan. to May. of the year n , 5 months
Analysis years	Jul. 1970 to Jun. 2005, 35 years for each member	Jun. of the year n to May. of the year $n+1$, 1 years for each member
Total samples Ensemble × years	8×35=280	26×1=26

Table 2. The climate responses of deforestation in the ocean feedback model test. The magnitudes listed below are the spatial-average in the land region in the Maritime Continent. Asterisks represent the values that pass the significance test.

Experiment	Variables	CTL	ANO
PreOcean	Precipitation (Wm^{-2})	248.75	19.60*
	Sensible heat flux (Wm^{-2})	27.90	15.84*
	Latent heat flux (Wm^{-2})	106.38	-30.11*
	Surface temperature (K)	298.01	3.26*
	Bowen ratio	0.31	0.37*
CpOcean minus PreOcean	Precipitation (Wm^{-2})	9.06*	-7.18
	Sensible heat flux (Wm^{-2})	4.06*	-2.40
	Latent heat flux (Wm^{-2})	-1.95*	3.15
	Surface temperature (K)	1.37*	-0.20
	Bowen ratio	0.05*	0.00
SbOcean minus PreOcean	Precipitation (Wm^{-2})	-5.88	-9.28
	Sensible heat flux (Wm^{-2})	1.62*	2.69
	Latent heat flux (Wm^{-2})	2.61*	-3.31
	Surface temperature (K)	0.96*	0.12
	Bowen ratio	0.02*	0.11

REFERENCES



Chang, C. P., Wang, Z., Ju, J. H., & Li, T. (2004). On the relationship between western maritime continent monsoon rainfall and ENSO during northern winter. *Journal of Climate*, 17(3), 665-672.

Chen, C. A., Yu, J. Y., & Chou, C. (2016). Impacts of Vertical Structure of Convection in Global Warming: The Role of Shallow Convection. *Journal of Climate*, 29(12), 4665-4684.

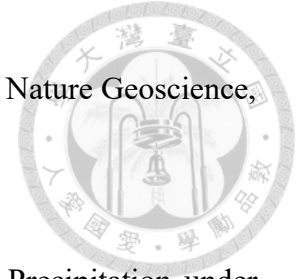
Chen, C. C., Lo, M. H., Im, E. S., Yu, J. Y., Liang, Y. C., Chen, W. T., Tang, I. P., Lan, C. W., Wu, R. J., & Chien, R. Y. (2019). Thermodynamic and Dynamic Responses to Deforestation in the Maritime Continent: A Modeling Study. *Journal of Climate*, 32(12), 3505-3527.

Chen, H. C., Lo, M. H. Contrasting Responses of Surface Heat Fluxes to Tropical Deforestation. Manuscript submitted for publication.

Chen, L., & Dirmeyer, P. A. (2020). Reconciling the disagreement between observed and simulated temperature responses to deforestation. *Nature Communications*, 11(1).

Chen, L., Ford, T. W., & Yadav, P. (2021). The role of vegetation in flash drought occurrence: A sensitivity study using community earth system model, version 2. *Journal of Hydrometeorology*, 22(4), 845-857.

Chou, C., Chiang, J. C. H., Lan, C. W., Chung, C. H., Liao, Y. C., & Lee, C. J. (2013).



Increase in the range between wet and dry season precipitation. *Nature Geoscience*, 6(4), 263-267.

Chou, C., & Lan, C. W. (2012). Changes in the Annual Range of Precipitation under Global Warming. *Journal of Climate*, 25(1), 222-235.

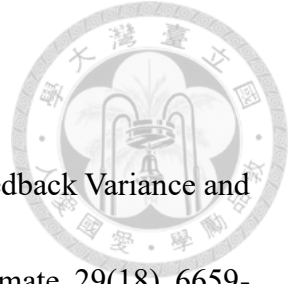
de Oliveira, J. V., Ferreira, D. B. D., Sahoo, P. K., Sodre, G. R. C., de Souza, E. B., & Queiroz, J. C. B. (2018). Differences in precipitation and evapotranspiration between forested and deforested areas in the Amazon rainforest using remote sensing data. *Environmental Earth Sciences*, 77(6).

Delire, C., Behling, P., Coe, M. T., Foley, J. A., Jacob, R., Kutzbach, J., Liu, Z., Vavrus, S. (2001). Simulated response of the atmosphere - ocean system to deforestation in the Indonesian Archipelago. *Geophysical Research Letters*, 28, 2081 - 2084

Dickinson, R. E., & Kennedy, P. (1992). Impacts on Regional Climate of Amazon Deforestation. *Geophysical Research Letters*, 19(19), 1947-1950.

Dirmeyer, P. A., & Shukla, J. (1994). Albedo as a Modulator of Climate Response to Tropical Deforestation. *Journal of Geophysical Research-Atmospheres*, 99(D10), 20863-20877.

Fujii, Y., Ishibashi, T., Yasuda, T., Takaya, Y., Kobayashi, C., & Ishikawa, I. (2021). Improvements in tropical precipitation and sea surface air temperature fields in a coupled atmosphere-ocean data assimilation system. *Quarterly Journal of the Royal*



Meteorological Society, 147(735), 1317-1343.

Gettelman, A., Lin, L., Medeiros, B., & Olson, J. (2016). Climate Feedback Variance and the Interaction of Aerosol Forcing and Feedbacks. *Journal of Climate*, 29(18), 6659-6675.

Halder, S., Saha, S. K., Dirmeyer, P. A., Chase, T. N., & Goswami, B. N. (2016). Investigating the impact of land-use land-cover change on Indian summer monsoon daily rainfall and temperature during 1951-2005 using a regional climate model. *Hydrology and Earth System Sciences*, 20(5), 1765-1784.

Henderson-Sellers, A., Dickinson, R. E., Durbidge, T. B., Kennedy, P. J., Mcguffie, K., & Pitman, A. J. (1993). Tropical Deforestation - Modeling Local-Scale to Regional-Scale Climate Change. *Journal of Geophysical Research-Atmospheres*, 98(D4), 7289-7315.

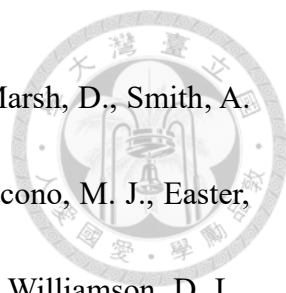
Lawrence, D., Coe, M., Walker, W., Verchot, L., & Vandecar, K. (2022). The Unseen Effects of Deforestation: Biophysical Effects on Climate. *Frontiers in Forests and Global Change*, 5.

Lawrence, D., & Vandecar, K. (2015). Effects of tropical deforestation on climate and agriculture. *Nature Climate Change*, 5(1), 27-36.

Lawrence, D. M., Oleson, K. W., Flanner, M. G., Thornton, P. E., Swenson, S. C., Lawrence, P. J., Zeng, X.-B., Yang, Z.-L., Levis, S., Sakaguchi, K., Bonan, G. B., &



- Slater, A. G. (2011). Parameterization improvements and functional and structural advances in Version 4 of the Community Land Model.
- Lee, T. H., & Lo, M. H. (2021). The role of El Nino in modulating the effects of deforestation in the Maritime Continent. *Environmental Research Letters*, 16(5).
- Lejeune, Q., Davin, E. L., Guillod, B. P., & Seneviratne, S. I. (2015). Influence of Amazonian deforestation on the future evolution of regional surface fluxes, circulation, surface temperature and precipitation. *Climate Dynamics*, 44(9-10), 2769-2786.
- Liu, H. W., Yu, J. Y., & Chen, C. A. (2018). Changes of tropical precipitation and convective structure under global warming projected by CMIP5 model simulations. *Terrestrial Atmospheric and Oceanic Sciences*, 29(4), 429-440.
- McBride, J. L., Haylock, M. R., & Nichols, N. (2003). Relationships between the maritime continent heat source and the El Nino-Southern Oscillation phenomenon. *Journal of Climate*, 16(17), 2905-2914.
- Mcguffie, K., Henderson-Sellers, A., Zhang, H., Durbridge, T. B., & Pitman, A. J. (1995). Global Climate Sensitivity to Tropical Deforestation. *Global and Planetary Change*, 10(1-4), 97-128.
- Messie, M., & Chavez, F. (2011). Global Modes of Sea Surface Temperature Variability in Relation to Regional Climate Indices. *Journal of Climate*, 24(16), 4314-4331.



Neale, R. B., Gettelman, A., Park, A., Conley, A. J., Kinnison, D., Marsh, D., Smith, A. K., Vitt, F., Morrison, H., Cameron-smith, P., Collins, W. D., Iacono, M. J., Easter, R. C., Liu, X.-H., Taylor, M. A., Chen, C.-C., Lauritzen, P. H., Williamson, D. L., Garcia, R., . . . Rasch, P. J. (2012). Description of the NCAR community atmosphere model (CAM 5.0).

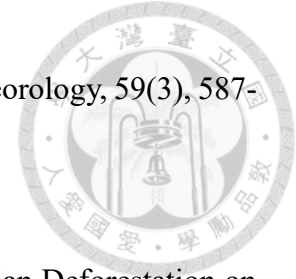
Neelin, J. D., & Held, I. M. (1987). Modeling Tropical Convergence Based on the Moist Static Energy Budget. *Monthly Weather Review*, 115(1), 3-12.

Nobre, C. A., Sellers, P. J., & Shukla, J. (1991). Amazonian Deforestation and Regional Climate Change. *Journal of Climate*, 4(10), 957-988.

Nogherotto, R., Coppola, E., Giorgi, F., & Mariotti, L. (2013). Impact of Congo Basin deforestation on the African monsoon. *Atmospheric Science Letters*, 14(1), 45-51.

Oleson, W. B., Lawrence, M., Bonan, B., Flanner, G., Kluzek, E., Lawrence, J., Levis, S., Swenson, C.L., Thornton, E., Dai, A., Decker, M., Dickinson, R.E., Feddema, J.J., Heald, L., Hoffman, F.M., Lamarque, J., Mahowald, N.M., Niu, G., Qian, T., Randerson, J.T., Running, S.W., Sakaguchi, K., Slater, A.G., Stöckli, R., Wang, A., Yang, Z., Zeng, X., & Zeng, X. (2010). Technical description of version 4.0 of the Community Land Model (CLM).

Pielke, R. A., Adegoke, J., Beltran-Przekurat, A., Hiemstra, C. A., Lin, J., Nair, U. S., Niyogi, D., & Nobis, T. E. (2007). An overview of regional land-use and land-cover



impacts on rainfall. *Tellus Series B-Chemical and Physical Meteorology*, 59(3), 587-601.

Polcher, J., & Laval, K. (1994). The Impact of African and Amazonian Deforestation on Tropical Climate. *Journal of Hydrology*, 155(3-4), 389-405.

Rayner, N. A., Parker, D. E., Horton, E. B., Folland, C. K., Alexander, L. V., Rowell, D. P., Kent, E. C., & Kaplan, A. (2003). Global analyses of sea surface temperature, sea ice, and night marine air temperature since the late nineteenth century. *Journal of Geophysical Research-Atmospheres*, 108(D14).

Reynolds, R. W., Smith, T. M., Liu, C., Chelton, D. B., Casey, K. S., & Schlax, M. G. (2007). Daily high-resolution-blended analyses for sea surface temperature. *Journal of Climate*, 20(22), 5473-5496.

Schneck, R., and Mosbrugger, V. (2011). Simulated climate effects of Southeast Asian deforestation: Regional processes and teleconnection mechanisms, *Journal of Geophysical Research*, 116, D11116

Tölle, M. H., Engler, S., & Panitz, H. J. (2017). Impact of Abrupt Land Cover Changes by Tropical Deforestation on Southeast Asian Climate and Agriculture. *Journal of Climate*, 30(7), 2587-2600.

Trenberth, K. E. (1997). The definition of El Nino. *Bulletin of the American Meteorological Society*, 78(12), 2771-2777.

Xue, P., Malanotte-Rizzoli, P., Wei, J., & Eltahir, E. (2020). Coupled Ocean-Atmosphere Modeling Over the Maritime Continent: A Review. *Journal of Geophysical Research: Oceans*, 125(6).

Zheng, T., Feng, T., Xu, K., & Cheng, X. H. (2020). Precipitation and the Associated Moist Static Energy Budget off Western Australia in Conjunction with Ningaloo Nino. *Frontiers in Earth Science*, 8.